# Enhanced optical nonlinearity in a silicon–organic hybrid slot waveguide for all-optical signal processing

Yonghua Wang,[1] ⓘ Su He,[1] Xiaoyan Gao,[2] Piaopiao Ye,[1] Lei Lei,[1,4] Wenchan Dong,[2,3,5] Xinliang Zhang,[2,3] and Ping Xu[1]

[1]College of Physics and Optoelectronic Engineering, Shenzhen University, Shenzhen 518060, China
[2]School of Optical and Electronic Information, Huazhong University of Science and Technology, Wuhan 430074, China
[3]Wuhan National Laboratory for Optoelectronics, Huazhong University of Science and Technology, Wuhan 430074, China
[4]e-mail: leilei@szu.edu.cn
[5]e-mail: wcdong@hust.edu.cn

Silicon photonic integrated devices used for nonlinear optical signal processing play a key role in ultrafast switching, computing, and modern optical communications. However, current devices suffer from limited operation speeds and low conversion efficiencies due to the intrinsically low nonlinear index of silicon. In this paper, we experimentally demonstrate enhanced optical nonlinearity in a silicon–organic hybrid slot waveguide consisting of an ultranarrow slot waveguide coated with a highly nonlinear organic material. The fabricated slot area is as narrow as 45 nm, which is, to the best of our knowledge, the narrowest slot width that has been experimentally reported in silicon slot waveguides. The nonlinear coefficient of the proposed device with a length of 3 mm is measured to be up to $1.43 \times 10^6$ $W^{-1}$ $km^{-1}$. Based on the nanostructure design, the conversion efficiencies of degenerate four-wave mixing showed enhancements of more than 12 dB and 5 dB compared to those measured for an identical device without the organic material and a silicon strip waveguide, respectively. As a proof of concept, all-optical canonical logic units based on the prepared device with two inputs at 40 Gb/s are analyzed. The obtained logic results showed clear temporal waveforms and wide-open eye diagrams with error-free performance, illustrating that our device has great potential for use in high-speed all-optical signal processing and high-performance computing in the nodes and terminals of optical networks. © 2021 Chinese Laser Press

https://doi.org/10.1364/PRJ.439251

## 1. INTRODUCTION

Optical nonlinearities are indispensable for all-optical signal processing in fast computing and communication applications [1,2]. In these application cases, the nonlinearities are not suppressed as in optical transmission applications, but instead, they are utilized, and it is therefore desirable to make highly nonlinear devices. All-optical signal processing has been studied in various highly nonlinear media that leverage different nonlinear processes, such as highly nonlinear optical fibers [3–5], optical semiconductor amplifiers [6], and periodically poled lithium niobate devices [7,8]. Among these nonlinear devices, silicon photonic integrated devices have attracted significant attention due to their advantages of compact footprints and compatibility with complementary metal–oxide-semiconductor platforms [9–12], as well as their low power consumption, which can help mitigate the ballooning energy requirements of modern-day network infrastructures.

Although silicon has been a prominent platform for integrated photonic devices, its strong two-photon absorption (TPA) at near-infrared wavelengths [13] and the associated TPA-induced free carrier absorption (FCA) limit the operating speeds of silicon-based photonic devices [14,15]. This absorption partially reduces the optical intensity in the devices, and in turn, decreases the generation or conversion efficiency of the nonlinear effects. To overcome this inherent limitation of silicon-based devices, a hybrid silicon–organic strategy, which combines the advantages of silicon with the ultrafast performance of organic materials, has attracted growing attention. Compared to silicon, organic material benefits from large nonlinear susceptibility and negligible nonparametric processes such as TPA and FCA. These outstanding features make organic materials attractive in the development of silicon–organic hybrid (SOH) photonic devices [16–23]. One promising application is the electro-optical (EO) modulation based on

EO polymer and strong Pockels (linear EO) or Kerr (quadratic EO) effect [17–21]. SOH nanostructures are still popular in ultrafast optical signal processing using enhanced third-order nonlinearity [22,23], which is also what we focus on in this work. In particular, by using silicon–organic slot structures, the nonlinearity can be greatly improved through efficient optical field confinement in nano-gaps filled with a highly nonlinear organic material [23]. For this kind of structure, achieving high nonlinearity requires two design aspects. One is the width of the nano-gap. A narrower slot usually enables a more intense optical field confinement. Based on the commonly used 220 nm or 250 nm silicon-on-insulator (SOI) wafer, most of the reported slot waveguides have slot widths larger than 70 nm since an ultranarrow slot often requires a high aspect ratio [24,25], which makes the fabrication challenging. The second design aspect is that the selected organic material needs to have a high Kerr index. So far, to realize high-efficiency third-order nonlinearity, poly(2,4-hexadiyne-1,6-diol di-p-toluenesulfonate) (PTS) and 2-[4-(dimethylamino)phenyl]-3-[4-(dimethylamino)phenyl] ethynyl buta-1,3-diene-1,1,4,4-tetracarbonitrile (DDMEBT) are most often used in the reported silicon–organic slot waveguides, and exhibit nonlinear indices of $2 \times 10^{-16}$ m$^2$/W [26] and $1.7 \times 10^{-17}$ m$^2$/W around 1550 nm, respectively [27]. Even though these two organic materials have good nonlinear indices, both require additional synthesis steps and complicated device fabrication [28,29]. Thus, the whole fabrication process is not efficient and is usually difficult to replicate.

In this work, we propose and experimentally demonstrate a highly nonlinear SOH slot waveguide (SOHSW) with a nonlinear coefficient higher than $1.43 \times 10^6$ W$^{-1}$ km$^{-1}$. The fabricated silicon slot is as narrow as 45 nm. To the best of our knowledge, this is the narrowest silicon slot waveguide that has ever been experimentally reported. The nonlinear organic material 2-methoxy-5-(2-ethylhexyloxy)-1,4-phenylenevinylene (MEH-PPV), whose Kerr index is measured as $(8.5 \pm 0.4) \times 10^{-17}$ m$^2$/W at 1550 nm by the Z-scan method, is filled into the ultranarrow slot where the propagating light is confined and enhanced significantly. Compared to an identical nanostructure without the organic material film and a silicon strip waveguide, the conversion efficiency of degenerate four-wave mixing (DFWM) observed in our SOHSW increases over 12 dB and 5 dB, respectively. To explore the application potential of the SOHSW in high-speed optical signal processing, 40 Gb/s two-input canonical logic units are experimentally demonstrated with error-free performance as a proof of concept. The proposed nanostructure could be attractive in future optical networks for its high nonlinearity, ease of implementation in both polymer formulation and waveguide fabrication, as well as potential use for ultrafast optical communication and optical high-performance computing.

## 2. DEVICE DESIGN AND FABRICATION

### A. Device Design and Nonlinear Coefficients

The proposed SOHSW based on a 220 nm SOI wafer is illustrated in Fig. 1(a). The slot waveguide is a classic light-field enhancement structure, in which light confinement is achieved by introducing a large discontinuity in the electric field at high-index-contrast interfaces. This confinement results in a strong enhancement of the field in the slot area [30]. The mode profile of the SOHSW made with a 300 nm thick nonlinear polymer layer ($h_p$) is shown in Fig. 1(b), and Fig. 1(c) shows the corresponding normalized magnitude of $E$. As seen in Figs. 1(b) and 1(c), the light is confined in the nano-scale nonlinear organic slot, which leads to slight TPA and associated FCA within the silicon due to the relatively weak power density [31].
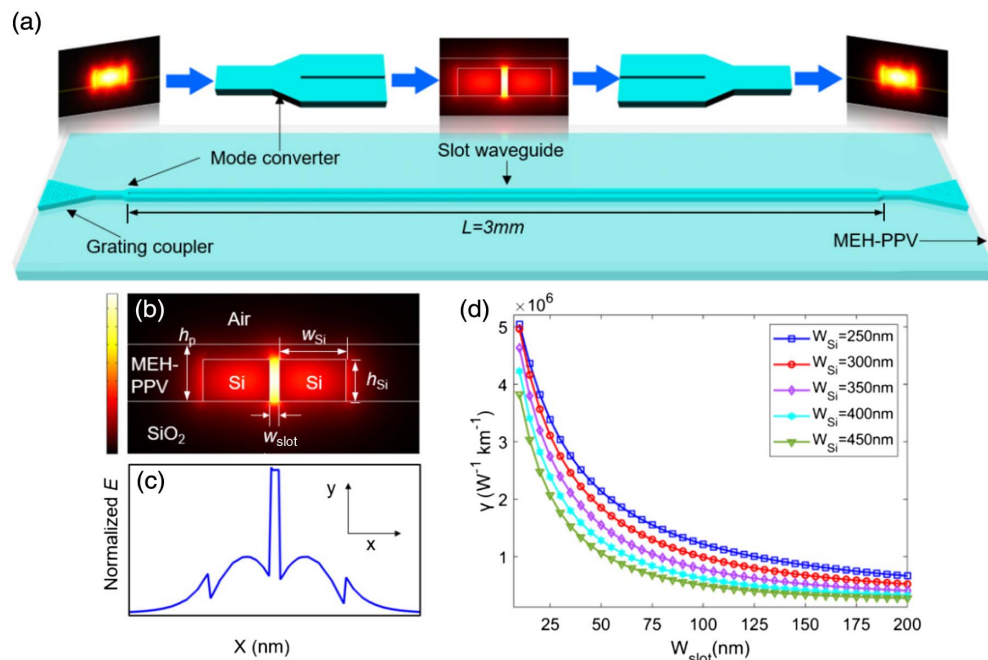


**Fig. 1.** (a) Schematic diagram of the highly nonlinear SOHSW. (b) Normalized electric field distribution and (c) corresponding normalized magnitude of the SOHSW. (d) Evolution of the nonlinear coefficient $\gamma$ with various slot widths for different waveguide widths.

**Table 1. Parameters Used to Calculate the Effective Nonlinear Coefficient of the SOHSW**

| Material | $n$ | $n_2$ (m$^2$/W) | $A_{\text{eff}}$ (µm$^2$) |
|---|---|---|---|
| MEH-PPV | 1.65 | $4.5 \times 10^{-17}$ | 0.019133 |
| Si | 3.48 | $5.3 \times 10^{-18}$ | 0.120470 |
| SiO$_2$ | 1.48 | $4.7 \times 10^{-20}$ | 0.051590 |

The nonlinear coefficient of the SOHSW is estimated for each material in the slot waveguide and scaled via the respective fractional energy $E_{f,q}$ of the material. The effective nonlinear coefficient $\gamma$ can be expressed as

$$\gamma = \sum \gamma_q \cdot E_{f,q}, \qquad (1)$$

with $\gamma_q$ defined as

$$\gamma_q = \frac{\omega n_2}{c A_{\text{eff}}}, \qquad (2)$$

where $\omega$ is the angular frequency of the incident light, $n_2$ is the Kerr index of the material, and $A_{\text{eff}}$ denotes the effective mode area defined as $A_1$ in Ref. [32]. The parameters used to estimate $\gamma$ of the SOHSW are presented in Table 1 [31,33]. The evolution of the estimated $\gamma$ with varying slot widths ($w_{\text{slot}}$) is calculated for waveguide widths ($w_{\text{Si}}$) ranging from 250 nm to 450 nm, as depicted in Fig. 1(d). It is seen that for all waveguide widths, $\gamma$ strongly depends on $w_{\text{slot}}$, where $\gamma$ is exponentially attenuated with increasing $w_{\text{slot}}$. The improvement in $\gamma$ is particularly significant when $w_{\text{slot}}$ is less than 50 nm due to the

increasingly tight optical field confinement. Also, the overall magnitude of the entire curve increases as the width of the waveguide decreases. This is ascribed to the comparatively higher fractional energy in the MEH-PPV cladding associated with the lower total energy in the device when the silicon waveguide gets narrower. It is worth noting that for plasmonic waveguides, since the metal layer is thin (i.e., around 20–40 nm), an ultranarrow slot width less than 30 nm can be obtained using a liftoff technique after an electron beam lithography (EBL) process [31,34,35]. While in silicon nanostructures, the slot area is usually fabricated using inductively coupled plasma (ICP) etching, and it is challenging to fully etch an ultranarrow slot (i.e., less than 70 nm) due to the high aspect ratio. Taking the practical fabrication conditions into account, the final designed geometry of the waveguide in this work is $w_{\text{slot}} = 50$ nm, $w_{\text{Si}} = 350$ nm, and $h_p = 300$ nm.

**B. Nonlinearity Measurement of MEH-PPV**

The MEH-PPV cladding layer is created by first dissolving 20 mg of MEH-PPV powder (Shanghai Aladdin Biochemical Technology Co., Ltd., average molecular weight 70,000–100,000) into 1.5 mL of toluene. The solution is then magnetically stirred at a temperature of 70°C for 24 h. To create the MEH-PPV cladding sample, the MEH-PPV solution is spin coated onto a silica wafer to produce a 0.8 µm film. The nonlinear characteristics of the MEH-PPV film are measured using the Z-scan method [33]. The experimental setup is depicted in Fig. 2(a). An input Gaussian laser beam is obtained using a femtosecond laser (Carbide CB5, pulse width 216 fs,
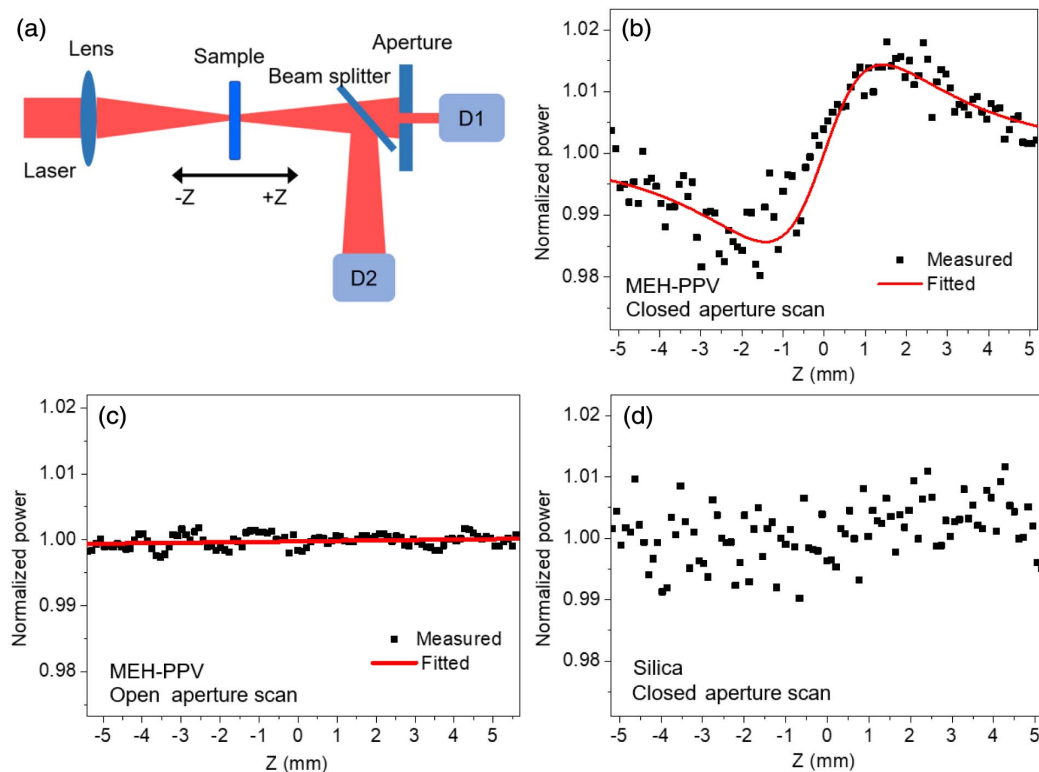


**Fig. 2.** (a) Experimental setup for the Z-scan measurement. (b) Closed aperture scan of a 0.8 µm thick MEH-PPV film with 1 mm thick fused silica substrate. (c) Open aperture scan of the MEH-PPV film for absorption measurement. (d) Closed aperture scan of a 1 mm thick fused silica substrate.

repetition frequency 1 kHz) at a wavelength of 1030 nm, and the wavelength is converted to 1550 nm by an optical parametric amplifier. The converted beam is focused through a convex lens (focal length 200 mm) and transmitted through the sample into a beam splitter. The transmission branch is received through a finite aperture in the far field and detected by detector D1 to measure the nonlinear index, while the reflected branch is received by detector D2, which does not contain an aperture to measure the nonlinear absorption. On both detectors, the transmittance of MEH-PPV is measured as a function of the sample position $z$ with respect to the focal plane. In the following, we will refer to the measurement of the nonlinear index as the "closed aperture scan" and the nonlinear absorption measurement as the "open aperture scan."

One condition that must be met when making the open aperture scan in the far field region is that the distance from the sample to the aperture must be far greater than the Rayleigh length of the beam. In this case, the nonlinear index $n_2$ of the material can be calculated using [36]

$$T = 1 - \frac{4\Delta\Phi_0 x}{(x^2 + 9)(x^2 + 1)}, \tag{3}$$

$$\Delta\Phi_0 = \frac{2\pi n_2 I_0 L_{\text{eff}}}{\lambda}, \tag{4}$$

$$L_{\text{eff}} = (1 - e^{-\alpha L})/\alpha, \tag{5}$$

where $T$ is the normalized transmission, $\Delta\Phi_0$ is the nonlinear phase change, $x$ is the ratio between the scan length $z$ and the Rayleigh length of the beam $z_0$ (i.e., $x = z/z_0$), $I_0$ denotes the on-axis intensity at the focal point, and $\lambda$ is the beam wavelength. $L$ and $L_{\text{eff}}$ refer to the real and effective sample thicknesses, respectively, and $\alpha$ is the linear absorption coefficient.

The experimental settings of the Z-scan of the MEH-PPV film are shown in detail in Table 2. Figure 2(b) illustrates the data collected during the closed aperture scan of a 0.8 µm thick MEH-PPV film on a 1 mm thick fused silica substrate at the peak intensity of $I_0 = 29.1 \text{ GW/cm}^2$. It is observed from Fig. 2(b) that the normalized power clearly shows a valley–peak configuration, which confirms that nonlinear refraction occurs in the sample, and the nonlinear index $n_2$ of the MEH-PPV is positive (self-focusing). For the open aperture scan shown in Fig. 2(c), it is seen that the received normalized power is flat and displays neither a valley nor a peak, indicating nonlinear absorption in the MEH-PPV film is negligible. This lack of nonlinear absorption is then further verified by increasing the laser power to a peak intensity of 40 GW/cm² at the focal point, which is adequate for the nonlinear absorption measurement and close to the damage threshold of MEH-PPV. The power evolution measured in this case is again steady, which further supports our conclusion that there is negligible nonlinear absorption. Based on the device design, the power intensity

in the proposed slot with an area of 0.22 µm × 0.045 µm is estimated to be 1 GW/cm² for an input average power of 100 mW, which is much lower than that set in the Z-scan measurement. This calculation confirms that nonlinear absorption in the slot area of the proposed SOHSW can be ignored.

To estimate the influence of the silica substrate on the nonlinear index of the polymer, we also measure a closed aperture scan of a bare 1 mm thick silica substrate with the same peak intensity as shown in Fig. 2(d). The results of this measurement show that the nonlinear refraction in the fused silica is extremely weak and support that it is reasonable to attribute the nonlinear refraction to the MEH-PPV film only. Based on the above measurements and Eqs. (3)–(5), the nonlinear index of MEH-PPV is calculated to be $(8.5 \pm 0.4) \times 10^{-17} \text{ m}^2/\text{W}$, which is almost 20 times the value of silicon [10].

## C. Fabrication of the SOHSW

The device is fabricated on a standard SOI wafer with a silicon thickness of 220 nm and a buried-oxide thickness of 2 µm. Figure 3(a) illustrates the fabrication steps used to create the SOHSW. The device pattern is transferred to the silicon layer using EBL and ICP etching. For the lithography steps [step i in Fig. 3(a)], we use a high-resolution nanolithography system (Raith EBPG5150) to obtain an ultranarrow slot. In addition, to obtain both high precision and a high-etching selection ratio, a positive high-contrast e-beam resist ARP-6200 (CSA-62) is adopted as the mask. The difficulty to create an ultranarrow slot area relies on the etching gas diffusion in the nano slot with a high aspect ratio, as well as the etching rate ununiformity induced by the loading effect depending on the different feature sizes. Specifically, for the silicon waveguide based on the 220 nm SOI wafer, the etching region on each side of the nanostructure is usually as wide as a few micrometers (i.e., ① ② in step ii), which is much wider than the slot width. Thus, during etching, the etching gas diffuses more slowly in the narrow slot than on both sides, resulting in a slower etching rate of the slot correspondingly. In this case, when the side regions reach the depth of 220 nm, the slot depth is still less than 220 nm. This issue is well resolved in our fabrication by over etching the substrate (ii and iii) and fine-tuning the etching recipe. In this way, the side regions are over etched into the silica layer where the side regions are slightly deeper than 220 nm, while the slot can just be fully etched. Note that the over etching, however, will not affect the light transmission much since the refractive index of MEH-PPV is close to that of silica. In addition, the etching rate of silica is much lower than that of silicon so that the over etched substrate will not be too deep in our fabrication. Another important point is that the thickness of the photoresist should be well optimized. If the photoresist is too thin, the silicon waveguide might also be etched during the over etching process, while if too thick, the resolution of the e-beam lithography would be reduced due to the electron scattering and proximity effect. Thus, the resist thickness, lithography parameters, and etching parameters need to be comprehensively optimized to obtain the ultranarrow slot. In our fabrication, the 45 nm narrow slot is successfully achieved with the following fabrication parameters: (1) 400 nm thick photoresist ARP-6200; (2) EBL acceleration voltage of 100 kV, beam current of 0.5 nA, and exposure dose of 450 µC/cm²; (3) ICP etching

**Table 2. Experimental Parameters for the Closed Aperture Scan**

| Input Power (µW) | $L$ (µm) | $\alpha$ (µm⁻¹) | $z_0$ (mm) | $I_0$ (GW/cm²) |
|---|---|---|---|---|
| 95.6 | 0.8 | 0.13 | 1.66 | 29.1 |
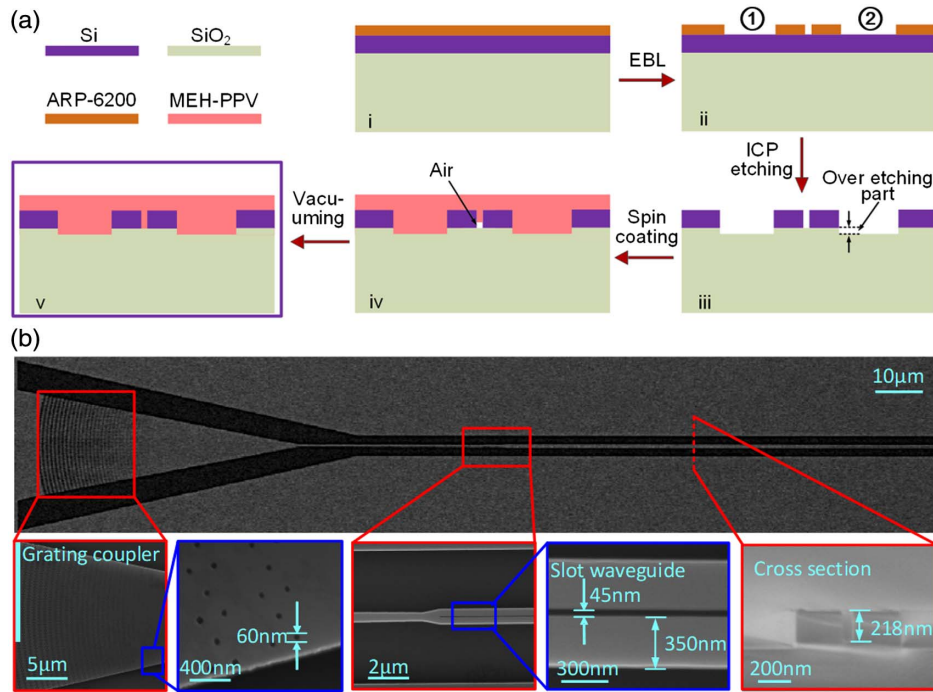
**Fig. 3.** (a) Illustration of the device fabrication steps of the presented SOHSW. (b) Scanning electron microscopy images of the fabricated device.

time of 160 s, and etching gas composed of 70 standard cubic centimeters per minute (sccm) of trifluoromethane ($CHF_3$), 10 sccm of sulfur-hexafluoride ($SF_6$), and 50 sccm of oxygen ($O_2$). The dissolved MEH-PPV is then spin coated on the chip at 2000 revolutions per second (RPS) to create a 250 nm film (iv). Any air remaining in the ultranarrow slot is then removed under vacuum to ensure that the organic material fully fills the slot (v). Scanning electron microscopy (SEM) images of the SOHSW are shown in Fig. 3(b). Photonic crystal apodized grating couplers with an initial aperture of 60 nm are used for input and output coupling. The images show that the fabricated SOHSW matches the design, and the measured $w_{slot}$, $w_{Si}$ and slot depths are 45 nm, 350 nm, and 218 nm, respectively.

## 3. SYSTEM EXPERIMENTS

### A. Enhanced Nonlinear Coefficient of the SOHSW

The nonlinear performance of the SOHSW is characterized by assessing the conversion of DFWM with two continuous waves (CWs) [23], of which the stronger wave is referred to as the pump, while the weaker one is the signal. Figure 4(a) shows the corresponding experimental setup. Two CW beams (Alnair Labs, TLG-200) with respective wavelengths of 1542.5 nm (P1) and 1544.1 nm (S1) are amplified and then multiplexed with the input grating coupler in the SOHSW. A polarization controller (PC) is used in each channel after the amplification to optimize the incident CW polarization in the transverse electric (TE) mode. The average powers of P1 and S1 measured at the output of the dense wavelength division multiplexer (DWDM) are 24 dBm and 19 dBm, respectively. Taking the coupling loss of 5 dB/facet into account, the respective average powers of the two pumps involved in the SOHSW are 19 dBm

and 14 dBm. The FWM performance is observed at the output grating coupler via an optical spectrum analyzer (OSA, Yokogawa, AQ6370D).

Based on the DFWM, the nonlinear coefficient $\gamma$ of the waveguide can be determined as follows [23]:

$$\eta = e^{-\alpha L}(\gamma P_p L_{eff})^2, \tag{6}$$

where $\eta$ denotes the conversion efficiency of DFWM, which is defined as the ratio of the converted idler power with respect to the input signal power [37]. $\alpha$ is the linear propagation loss, $P_p$ is the pump power coupled into the waveguide, and $L$ and $L_{eff}$ refer to the real and effective waveguide lengths, respectively. $L_{eff}$ is further expressed as

$$L_{eff} = \frac{\sqrt{1 + e^{-2\alpha L} - 2e^{-\alpha L}\cos(\Delta\beta L)}}{\sqrt{\alpha^2 + \Delta\beta^2}}, \tag{7}$$

where $\Delta\beta$ is the phase mismatch between the signal and idler waves and can be calculated using a finite vectorial finite difference mode solver [38].

Figure 4(b) displays the FWM spectra measured for the SOHSW (red line) and the bare silicon slot waveguide without the MEH-PPV film (blue line). Both nanostructures have lengths of 3 mm. As illustrated in Fig. 4(b), the conversion efficiency using the SOHSW is measured as −27.5 dB, providing a 12.2 dB enhancement compared to that using the bare slot waveguide as shown in the magnified window. Apart from the slot waveguide, a comparison of the FWM performance of the SOHSW and strip waveguide is also demonstrated as shown in Fig. 4(c). The slot in the referenced strip waveguide is 220 nm high and 450 nm wide. In this case, the FWM conversion efficiencies of both idlers achieved with the SOHSW are more than 5 dB higher than those based on the strip waveguide.
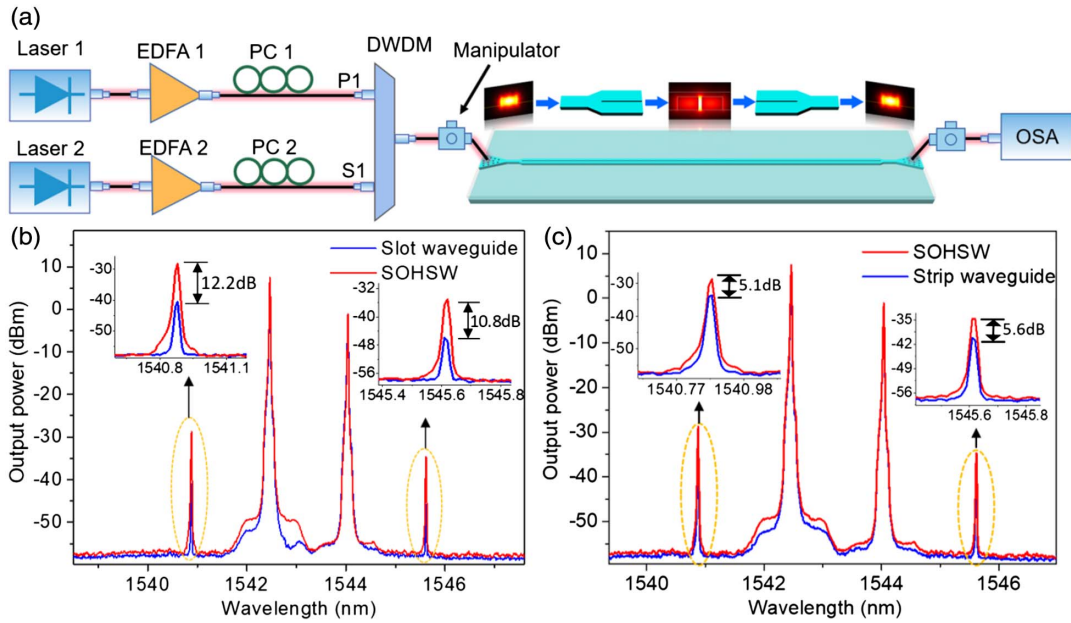
**Fig. 4.** (a) Experimental setup used to measure the nonlinear coefficients. (b) FWM spectra of the SOHSW (red curve) and bare silicon slot waveguide (blue curve). (c) FWM spectra of the SOHSW (red curve) and strip waveguide (220 nm × 450 nm, blue curve).

**Table 3. Parameters Used to Calculate $\gamma$ of the Three Waveguides**

| Waveguide | $L$ (mm) | $\Delta\beta$ (m$^{-1}$) | $P_p$ (dBm) | $\alpha$ (m$^{-1}$) | $\eta$ | $\gamma$ (W$^{-1}$ km$^{-1}$) |
|---|---|---|---|---|---|---|
| SOHSW | 3 | 4.56 | 19 | 767 | 0.0018 | $1.43 \times 10^6$ |
| Slot waveguide | 3 | 10.53 | 18.5 | 732 | 0.0001 | $3.52 \times 10^5$ |
| Strip waveguide | 3 | −0.80 | 17 | 87 | 0.0005 | $2.5 \times 10^5$ |

It is worth noting that for both cases, the nonlinearity enhancement could be even greater by reducing the scattering losses from the rough slot sidewalls via optimizing the fabrication conditions such as by including annealing and thermal oxidation steps. According to Eqs. (6) and (7), parameters used to determine the nonlinear coefficients of the three waveguides are given in Table 3, among which, the SOHSW exhibits an outstanding nonlinear coefficient of $1.43 \times 10^6$ W$^{-1}$ km$^{-1}$, while

the coefficient for the slot waveguide is $3.52 \times 10^5$ W$^{-1}$ km$^{-1}$ and for the strip waveguide is $2.5 \times 10^5$ W$^{-1}$ km$^{-1}$.

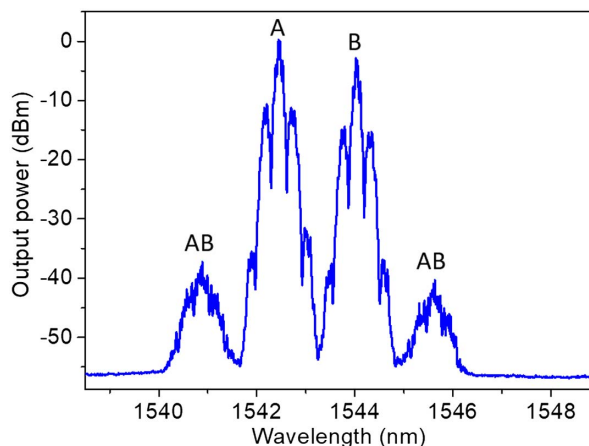## B. SOHSW for All-Optical High-Speed Logic Operations

The enhanced nonlinearity in the SOHSW makes the nanostructured device a good candidate for all-optical high-speed signal processing. Here, as a proof of concept, we
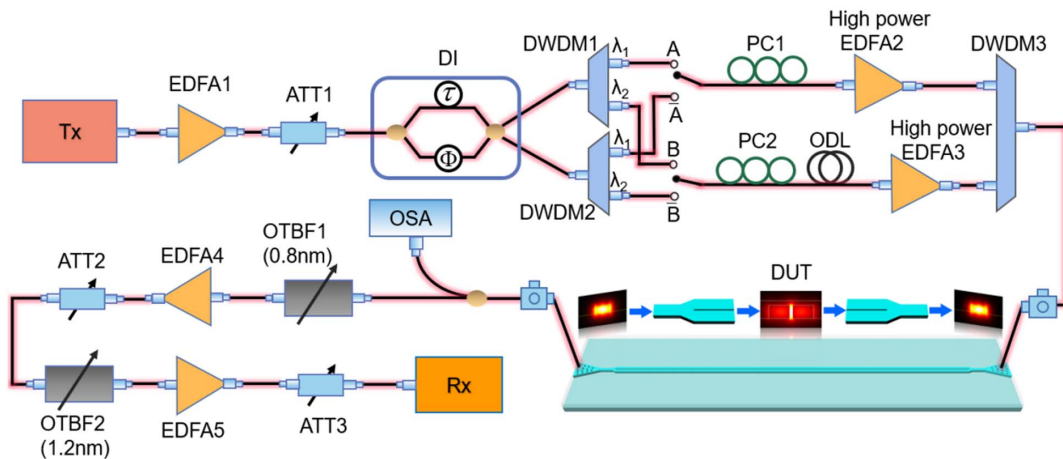


**Fig. 5.** Experimental setup for the 40 Gb/s all-optical logic canonical units based on the SOHSW.

experimentally demonstrate 40 Gb/s all-optical canonical logic units, performing as the basic building blocks for complexed reconfigurable logic functions. The experimental setup is shown in Fig. 5. Two return-to-zero differential phase-shift keying (RZ-DPSK) signals with a bit rate of 40 Gb/s and a duty cycle of 33% are generated using a transmitter (Tx) with a $2^7 - 1$ pseudorandom binary sequence (PRBS). The wavelengths of the two signals are 1542.46 nm and 1544.06 nm. The modulated signals are first adjusted to 0 dBm by an erbium doped optical fiber amplifier (EDFA1) and an attenuator (ATT1) for precoding in the delay interferometer (DI), from which the original and complementary data patterns can be simultaneously measured as the constructive and destructive outputs. Two DWDMs with a free-spectral range (FSR) of 1.6 nm are then used to separate the data streams. We use an optical delay line (ODL) on one path for decorrelating and aligning the signals. Either the original pattern or the complement can be selected as inputs to the SOHSW. PC1 and PC2 are applied to each channel to optimize the polarization state of the two signals. After amplification by the high-power EDFAs, the signals are multiplexed via DWDM3 and coupled into the SOHSW for FWM-based logic AND operation. Thus, by switching the input precoded data patterns, the whole set of canonical logic units can be achieved. At the output of DWDM3, the average power of the original data path is measured as 24 dBm, while the average power of the complement data path is 20 dBm. Outgoing signals coupled from the SOHSW are divided into two branches, of which 50% is observed by OSA for spectral analysis, and the remaining signal is used to extract the logic information contained in the converted idler at 1540.88 nm. To this end, we use a cascading filter and optical power optimization composed of tunable bandpass filters (TBPF1 and TBPF2), pre-amplifiers (EDFA4 and EDFA5) and ATT2 and ATT3. The 3 dB bandwidths of the TBPFs are 0.8 nm and 1.2 nm. The final optical power of the target idler measured before the receiver (Rx) is –7 dBm.

Figure 6 shows the measured spectrum of FWM created by signals A and B. One can see that the logic information, i.e., A AND B (AB), is multicasted to both idlers. According to
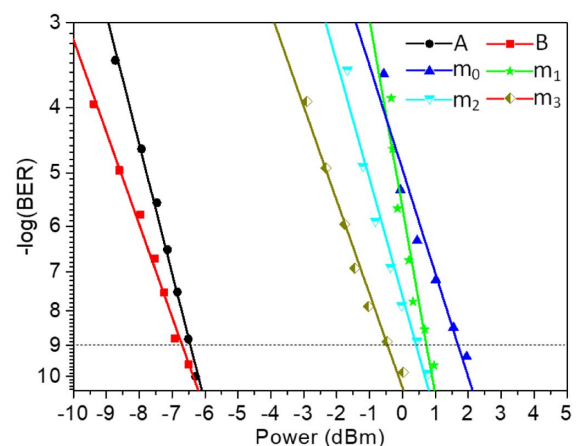
the spectrum, the conversion efficiency of the target idler is estimated as about –33 dB. As we discussed before, smoothing the sidewalls in the device slot by annealing or thermal oxidation could further increase the conversion efficiency.

Figures 7(a) and 7(b) illustrate the temporal waveforms of the original signals and logic results observed by the communication signal analyzer (CSA), respectively. It is found from Fig. 7 that the logic levels are clearly identified, and the logic sequences are correct with wide open eyes, resulting in extinction ratios higher than 12 dB. Additionally, as shown in Fig. 8, all logic results exhibit error-free performance with a power penalty less than –8 dB, which confirms the good performance of the logic operations and the promising use of SOHSW for high-speed signal processing as well.
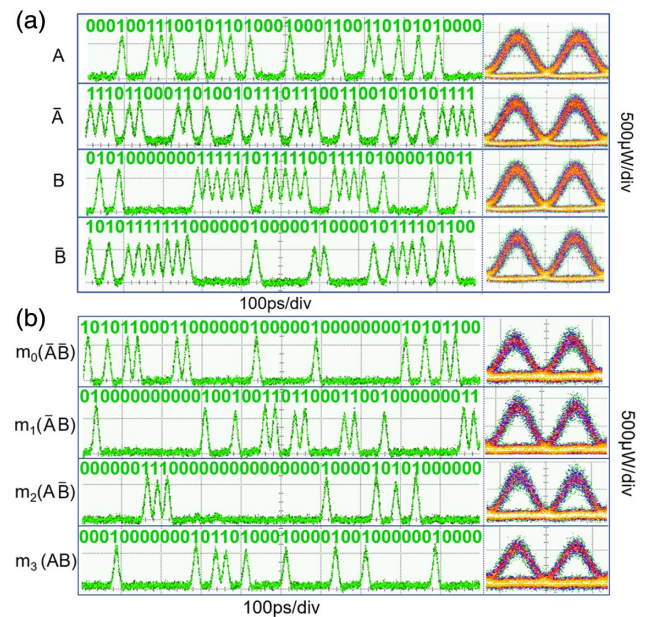


**Fig. 7.** Temporal waveforms and eye diagrams of the original signals and logical results.



**Fig. 6.** Measured FWM spectrum achieved at the output of SOHSW.



**Fig. 8.** Bit error rate (BER) measurements for the original signals and logic operations.

## 4. CONCLUSION

In summary, we propose and experimentally demonstrate a highly nonlinear silicon–organic slot waveguide for ultrafast all-optical signal processing and communication. Here, the nonlinearity of the chip is greatly enhanced by optical field confinement in a 45 nm wide slot that is filled with a nonlinear polymer MEH-PPV. To the best of our knowledge, this is the narrowest slot width that has ever been experimentally realized in silicon slot waveguides. Also, the organic polymer is easily obtained without the need for additional synthesis steps and also shows good nonlinear characteristics demonstrated by Z-scan. The nonlinear coefficient of SOHSW is then investigated through DFWM. The results show that the SOHSW offers obvious conversion efficiency enhancements of more than 12 dB and 5 dB compared to those achieved in a bare silicon slot waveguide and a strip waveguide, respectively. From the results, the nonlinear coefficient of the fabricated SOHSW is calculated to be as high as $1.43 \times 10^6$ $W^{-1}$ $km^{-1}$. To demonstrate the use of the prepared SOHSW in high-speed all-optical signal processing, we experimentally demonstrate its application in two-input canonical logic units at 40 Gb/s as a proof of concept. According to the obtained clear temporal waveforms, wide open eye diagrams, and error-free performance of the logic results, the proposed SOHSW shows promising prospects for use in ultrafast and large-capacity on-chip signal processing in future optical networks.

**Disclosures.** The authors declare no conflicts of interest.

**Data Availability.** The data that support the findings of this study are available from the corresponding author upon reasonable request.

## REFERENCES

1. I. L. Markov, "Limits on fundamental limits to computation," Nature **512**, 147–154 (2014).
2. A. E. Willner, S. Khaleghi, M. R. Chitgarha, and O. F. Yilmaz, "All-optical signal processing," J. Lightwave Technol. **32**, 660–680 (2014).
3. L. Lei, J. Dong, B. Zou, Z. Wu, W. Dong, and X. Zhang, "Expanded all-optical programmable logic array based on multi-input/output canonical logic units," Opt. Express **22**, 9959–9970 (2014).
4. G. Lu, T. Sakamoto, and T. Kawanishi, "Wavelength conversion of optical 64QAM through FWM in HNLF and its performance optimization by constellation monitoring," Opt. Express **22**, 15–22 (2014).
5. J. Qiu, K. Sun, M. Rochette, and L. R. Chen, "Reconfigurable all-optical multilogic gate (XOR, AND, and OR) based on cross-phase modulation in a highly nonlinear fiber," IEEE Photon. Technol. Lett. **22**, 1199–1201 (2010).
6. J. Qin, G. Lu, T. Sakamoto, K. Akahane, N. Yamamoto, D. Wang, C. Wang, H. Wang, M. Zhang, T. Kawanishi, and Y. Ji, "Simultaneous multichannel wavelength multicasting and XOR logic gate multicasting for three DPSK signals based on four-wave mixing in quantum-dot semiconductor optical amplifier," Opt. Express **22**, 29413–29423 (2014).
7. N. Deng, K. Chan, C. K. Chan, and L. K. Chen, "An all-optical XOR logic gate for high-speed RZ-DPSK signals by FWM in semiconductor optical amplifier," IEEE J. Sel. Top. Quantum Electron. **12**, 702–707 (2006).
8. J. Wang, J. Sun, and Q. Sun, "Single-PPLN-based simultaneous half-adder, half-subtracter, and OR logic gate: proposal and simulation," Opt. Express **15**, 1690–1699 (2007).
9. Q. Lin, O. J. Painter, and G. P. Agrawal, "Nonlinear optical phenomena in silicon waveguides: modeling and applications," Opt. Express **15**, 16604–16644 (2007).
10. M. Dinu, F. Quochi, and H. Garcia, "Third-order nonlinearities in silicon at telecom wavelengths," Appl. Phys. Lett. **82**, 2954–2956 (2003).
11. C. Koos, L. Jacome, C. Poulton, J. Leuthold, and W. Freude, "Nonlinear silicon-on-insulator waveguides for all-optical signal processing," Opt. Express **15**, 5976–5990 (2007).
12. E. Timurdogan, C. V. Poulton, M. J. Byrd, and M. R. Watts, "Electric field-induced second-order nonlinear optical effects in silicon waveguides," Nat. Photonics **11**, 200–206 (2017).
13. D. J. Moss, R. Morandotti, A. L. Gaeta, and M. Lipson, "New CMOS-compatible platforms based on silicon nitride and Hydex for nonlinear optics," Nat. Photonics **7**, 597–607 (2013).
14. R. Salem, M. A. Foster, A. C. Turner, D. F. Geraghty, M. Lipson, and A. L. Gaeta, "Signal regeneration using low-power four-wave mixing on silicon chip," Nat. Photonics **2**, 35–38 (2008).
15. J. Leuthold, C. Koos, and W. Freude, "Nonlinear silicon photonics," Nat. Photonics **4**, 535–544 (2010).
16. P. Steglich, C. Mai, C. Villringer, B. Dietzel, S. Bondarenko, V. Ksianzou, F. Villasmunta, C. Zesch, S. Pulwer, and M. Burger, "Silicon-organic hybrid photonics: an overview of recent advances, electro-optical effects and CMOS integration concepts," J. Phys. Photon. **3**, 022009 (2021).
17. P. Steglich, C. Mai, and A. Mai, "Silicon-organic hybrid photonic devices in a photonic integrated circuit technology," ECS J. Solid State Sci. Technol. **8**, Q217–Q221 (2019).
18. W. Heni, Y. Kutuvantavida, C. Haffner, H. Zwickel, C. Kieninger, S. Wolf, M. Lauermann, Y. Fedoryshyn, A. F. Tillack, L. E. Johnson, D. L. Elder, B. H. Robinson, W. Freude, C. Koos, J. Leuthold, and L. R. Dalton, "Silicon–organic and plasmonic–organic hybrid photonics," ACS Photon. **4**, 1576–1590 (2017).
19. J. Leuthold, W. Freude, J. M. Brosi, R. Baets, P. Dumon, I. Biaggio, M. L. Scimeca, F. Diederich, B. Frank, and C. Koos, "Silicon organic hybrid technology—a platform for practical nonlinear optics," Proc. IEEE **97**, 1304–1316 (2009).
20. J. Leuthold, C. Koos, W. Freude, L. Alloatti, R. Palmer, D. Korn, J. Pfeifle, M. Lauermann, R. Dinu, S. Wehrli, M. Jazbinsek, P. Gunter, M. Waldow, T. Wahlbrink, J. Bolten, H. Kurz, M. Fournier, J. M. Fedeli, Y. Hui, and W. Bogaerts, "Silicon-organic hybrid electro-optical devices," IEEE J. Sel. Top. Quantum Electron. **19**, 114–126 (2013).
21. Z. Xingyu, A. Hosseini, L. Xiaohui, H. Subbaraman, and R. T. Chen, "Polymer-based hybridintegrated photonic devices for silicon on-chip modulation and board-level optical interconnects," IEEE J. Sel. Top. Quantum Electron. **19**, 3401115 (2013).
22. T. W. Baehr-Jones and M. J. Hochberg, "Polymer silicon hybrid systems: a platform for practical nonlinear optics," J. Phys. Chem. C **112**, 8085–8090 (2008).
23. C. Koos, P. Vorreau, T. Vallaitis, P. Dumon, W. Bogaerts, R. Baets, B. Esembeson, I. Biaggio, T. Michinobu, F. Diederich, W. Freude, and J. Leuthold, "All-optical high-speed signal processing with silicon–organic hybrid slot waveguides," Nat. Photonics **3**, 216–219 (2009).
24. B. Arijit, K. Markku, H. Seppo, and R. Matthieu, "Silicon slot waveguide Fano resonator," Opt. Lett. **43**, 3489–3492 (2018).
25. S. Ummethala, J. N. Kemal, A. S. Alam, M. Lauermann, A. Kuzmin, Y. Kutuvantavida, S. H. Nandam, L. Hahn, D. L. Elder, L. R. Dalton, T. Zwick, S. Randel, W. Freude, and C. Koos, "Hybrid electro-optic

modulator combining silicon photonic slot waveguides with high-k radio-frequency slotlines," Optica **8**, 511–519 (2021).

26. B. L. Lawrence, M. Cha, J. U. Kang, W. Toruellas, G. Stegeman, G. Baker, J. Meth, and S. Etemad, "Large purely refractive nonlinear index of single crystal P-toluene sulphonate (PTS) at 1600 nm," Electron. Lett. **30**, 447–448 (1994).

27. S. Polyakov, F. Yoshino, M. Liu, and G. Stegeman, "Nonlinear refraction and multiphoton absorption in polydiacetylenes from 1200 to 2200 nm," Phys. Rev. B **69**, 115421 (2004).

28. M. T. Beels, M. S. Fleischman, I. Biaggio, B. Breiten, M. Jordan, and F. Diederich, "Compact TCBD based molecules and supramolecular assemblies for third-order nonlinear optics," Opt. Mater. Express **2**, 294–303 (2012).

29. J. Covey, A. D. Finke, X. Xu, W. Wu, Y. Wang, F. Diederich, and R. T. Chen, "All-optical switching with 1-ps response time in a DDMEBT enabled silicon grating coupler/resonator hybrid device," Opt. Express **22**, 24530–24544 (2014).

30. P. A. Anderson, B. S. Schmidt, and M. Lipson, "High confinement in silicon slot waveguides with sharp bends," Opt. Express **14**, 9197–9202 (2006).

31. M. P. Nielsen, X. Shi, P. Dichtl, S. A. Maier, and R. F. Oulton, "Giant nonlinear response at a plasmonic nanofocus drives efficient four-wave mixing," Science **358**, 1179–1181 (2017).

32. R. F. Oulton, G. Bartal, D. F. P. Pile, and X. Zhang, "Confinement and propagation characteristics of subwavelength plasmonic modes," New J. Phys. **10**, 105018 (2008).

33. M. Samoc, A. Samoc, and B. Luther-Davies, "Third harmonic autocorrelation and wave mixing in a thin film of poly(p-phenylenevinylene)," Opt. Express **11**, 1787–1792 (2003).

34. M. P. Nielsen, L. Lafone, A. Rakovich, T. Sidiropoulos, M. Rahmani, S. A. Maier, and R. F. Oulton, "Oulton Adiabatic nanofocusing in hybrid gap plasmon waveguide on the silicon-on-insulator platform," Nano Lett. **16**, 1410–1414 (2016).

35. M. Ono, M. Hata, M. Tsunekawa, K. Nozaki, H. Sumikura, H. Chiba, and M. Notomi, "Ultrafast and energy-efficient all-optical switching with graphene-loaded deep-subwavelength plasmonic waveguides," Nat. Photonics **14**, 37–43 (2020).

36. M. Sheik-Bahae, A. A. Said, T. Wei, D. J. Hagan, and E. W. Van Stryland, "Sensitive measurement of optical nonlinearities using a single beam," IEEE J. Quantum Electron. **26**, 760–769 (1990).

37. M. A. Foster, A. C. Turner, J. E. Sharping, B. S. Schmidt, M. Lipson, and A. L. Gaeta, "Broad-band optical parametric gain on a silicon photonic chip," Nature **441**, 960–963 (2006).

38. A. B. Fallahkhair, K. S. Li, and T. E. Murphy, "Vector finite difference modesolver for anisotropic dielectric waveguides," J. Lightwave Technol. **26**, 1423–1431 (2008).